ACS APPLIED MATERIALS & INTERFACES

Research Article

www.acsami.org

# Hierarchically Porous Carbon Nanosheets from Waste Coffee Grounds for Supercapacitors

Young Soo Yun,[†] Min Hong Park,[†] Sung Ju Hong,[‡] Min Eui Lee,[†] Yung Woo Park,[‡] and Hyoung-Joon Jin*,[†]

[†]Department of Polymer Science and Engineering, Inha University, Incheon 402-751, Korea

[‡]Department of Physics and Astronomy, Seoul National University, Seoul 151-747, South Korea

Supporting Information

**ABSTRACT:** The nanostructure design of porous carbon-based electrode materials is key to improving the electrochemical performance of supercapacitors. In this study, hierarchically porous carbon nanosheets (HP-CNSs) were fabricated using waste coffee grounds by in situ carbonization and activation processes using KOH. Despite the simple synthesis process, the HP-CNSs had a high aspect ratio nanostructure (~20 nm thickness to several micrometers in lateral size), a high specific surface area of 1945.7 $m^2$ $g^{-1}$, numerous heteroatoms, and good electrical transport properties, as well as hierarchically porous characteristics (0.5−10 nm in size). HP-CNS-based supercapacitors showed a specific energy of 35.4 Wh $kg^{-1}$ at 11250 W $kg^{-1}$ and of 23 Wh $kg^{-1}$ for a 3 s charge/discharge current rate corresponding to a specific power of 30000 W $kg^{-1}$. Additionally, the HP-CNS supercapacitors demonstrated good cyclic performance over 5000 cycles.

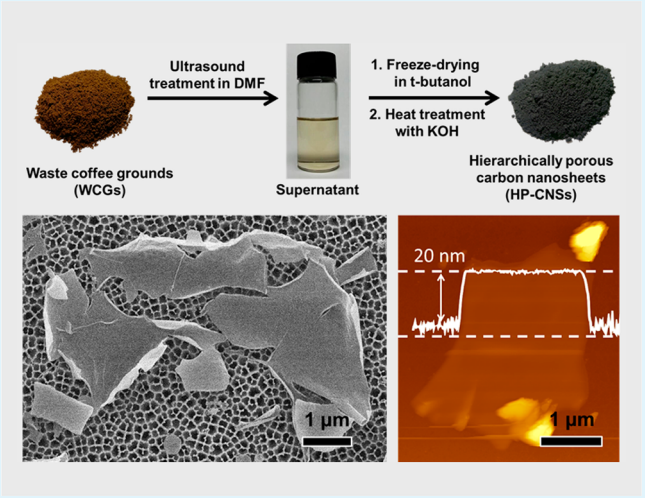


**KEYWORDS:** *waste coffee grounds, carbon nanosheet, porous carbon, supercapacitor*

## INTRODUCTION

Supercapacitors, also known as electrochemical capacitors, have attracted considerable attention for use in emerging applications such as electric vehicles, portable power tools, and uninterruptible power supplies due to their superior electrochemical performance, including high power capability, good reversibility, and long cycle life.[1] However, in contrast to batteries, supercapacitors have a low energy density (~5 Wh $kg^{-1}$), which has limited their use in many applications.[2] Additionally, currently available commercial supercapacitors do not have sufficient power to meet emerging needs.

The energy density of a supercapacitor is dependent on cell potential ($V$) and capacitance ($C$) according to $E = 1/2CV^2$; thus, a high capacitance and large operating cell voltage are required to increase the energy density of supercapacitors. The capacitance originates from pure electrostatic charge accumulation at the electrode/electrolyte interface. An increase in the electrode surface area that is accessible to electrolyte ions leads to greater capacitance.[3] Charge storage is also dependent on the surface properties and porosity of the electrodes (e.g., pore size). Ultramicropores (>1 nm) can contribute greater charge storage through electrolyte desolvation;[4] moreover, electrode wettability can further increase the number of active sites. In addition, the operating cell voltage can be increased using ionic liquid-based electrolytes, which has been demonstrated with carbon-based electrode materials.[5] The maximum power density ($P$) is given by $P_{max} = V_i^2/4R$, where $R$ is the equivalent series resistance. The power characteristics of supercapacitors are limited mainly by the ion delivery rate; hence, large pores that can act as an electrolyte reservoir, as well as ion pathways, are important considerations.[6]

High-performance supercapacitors require sophisticated electrode design that uses well-defined, tailored, carbon-based electrode materials with a hierarchical porous structure. Nanostructured carbon materials may satisfy this requirement due to their nanometer-sized effects (e.g., nanoionics[7] and nanoelectronics[8]) and the unusual properties originating from their confined dimensions.[9−12] The large surface-to-volume ratio leads to high energy and power characteristics through a large amount of surface charge storage and rapid mass transfer. Thus, various hierarchically porous nanostructured carbon materials (HP-NCMs) reportedly exhibit better performance suitable for supercapacitors.[13−21] High electrochemical performance has been achieved using HP-NCMs as electrodes for

Received: November 21, 2014
Accepted: January 22, 2015
Published: January 22, 2015





DOI: 10.1021/am5081919
ACS Appl. Mater. Interfaces 2015, 7, 3684−3690

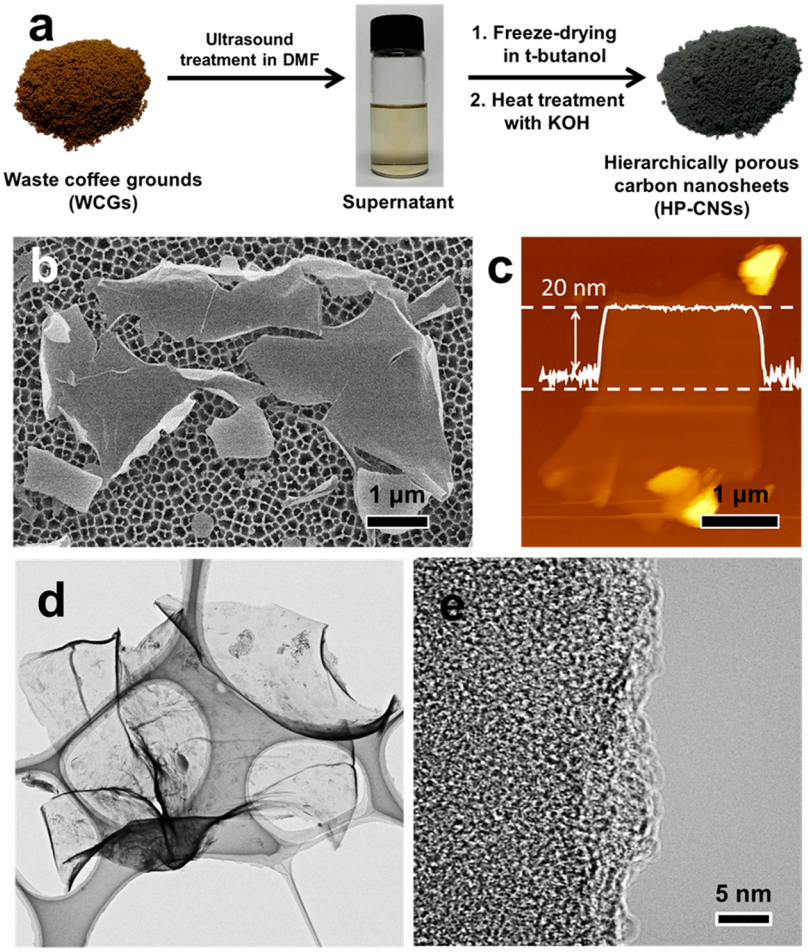


**Figure 1.** (a) Schematic diagram of the process for fabricating hierarchically porous carbon nanosheets (HP-CNSs). (b) A field-emission scanning electron microscopy (FE-SEM) image of HP-CNSs deposited on a porous alumina template. (c) An atomic force microscopy (AFM) image of HP-CNSs deposited on a Si wafer. (d, e) Field-emission transmission electron microscopy (FE-TEM) images of HP-CNSs deposited on a carbon grid at different magnifications.

supercapacitors; however, emerging applications require more power and energy, and the HP-NCM fabrication process is complicated and expensive.

Approximately 8 million metric tons of coffee, an important agricultural commodity, are produced globally each year;[22] most of this is discarded as waste coffee grounds (WCGs) by beverage manufacturers. WCGs are composed of primarily cellulose-based materials along with other components containing many heteroatoms (e.g., nitrogen, oxygen, and sulfur) that are considered to be good precursors for porous carbon material fabrication.[23−27] However, research in this area has been limited to activation processes, with little focus on nanostructure or hierarchical pore structure fabrication.

In this study, hierarchically porous carbon-based nanosheets (HP-CNSs) were fabricated from exfoliated WCGs using a KOH mixture through a simple, one-step heat treatment. The porous structure of the product could be easily controlled by adjusting the heat-treatment temperature (HTT) and the WCG to KOH ratio. The HP-CNSs exhibited unique material characteristics, and HP-CNS-based supercapacitors demonstrated superior electrochemical performance with high specific energy, high power, and cyclic stability.

## RESULTS AND DISCUSSION

Figure 1(a) shows a schematic diagram of the simple synthesis process used to generate HP-CNSs. Two-dimensional (2D)-type morphologies were observed in the supernatant of WCGs that were ultrasound-treated in *N*,*N*-dimethylformamide [Figure S1 in the Supporting Information (SI)]. The exfoliated WCGs exhibited an aliphatic carbon structure that was functionalized by various heteroatoms [Figure S2 in the SI] The heat treatment of exfoliated WCGs with KOH at 1200 °C transformed the $sp^3$ carbon structure of the WCGs into aromatic carbon structures containing numerous heteroatoms (e.g., 14.1, 4.1 and 0.9 atom % of oxygen, nitrogen, and sulfur, respectively, from X-ray photoelectron spectroscopy (XPS) analysis) [Figures S3 and S4 and Table S1 in the SI]. Additionally, amorphous and porous carbon structures were created via KOH activation and carbonization. A previous study showed that the activation of carbon by KOH involves two main mechanisms.[28] The first mechanism consists of the consumption of carbon by oxygen, which produces carbon monoxide and carbon dioxide that are catalyzed by alkali metals at temperatures below 700 °C.[29] Aromatization occurred at increasing HTTs in the WCG/KOH mixtures; thus, the basic structural unit (BSU) of the graphitic structure could develop gradually at temperatures below 700 °C.[30] The BSU produced is relatively stable for the activation process. Therefore, more


DOI: 10.1021/am5081919
ACS Appl. Mater. Interfaces 2015, 7, 3684−3690

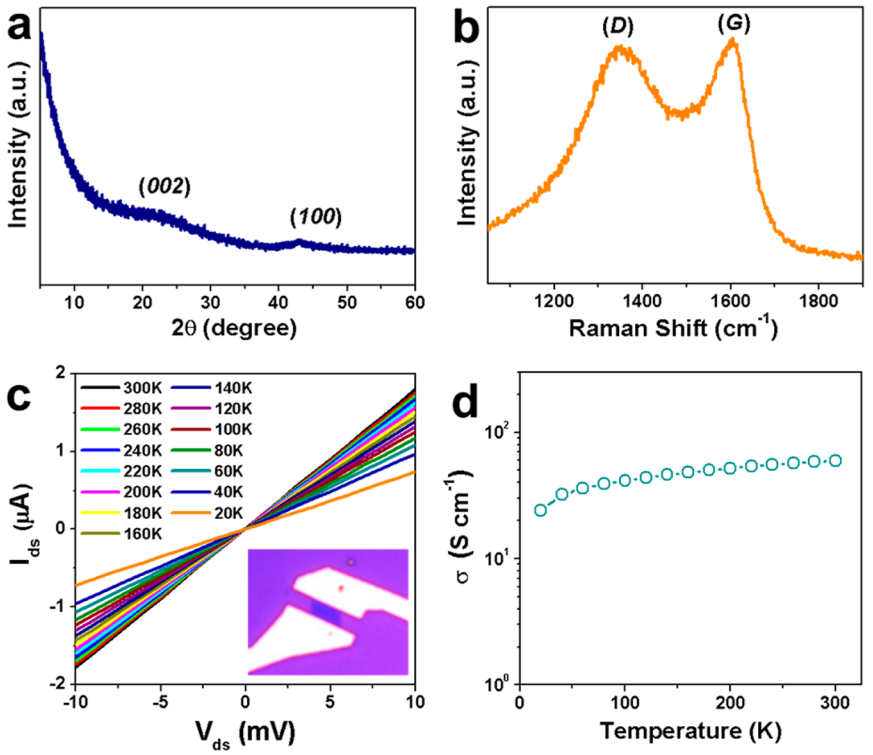


**Figure 2.** (a) X-ray diffraction (XRD) patterns, (b) Raman spectra, (c) temperature-dependent current−voltage ($I$−$V$) characteristics, and (d) the conductivity curve of HP-CNSs.

reactive carbon atoms can be continuously removed as carbon monoxide and carbon dioxide during the carbonization process. Above 700 °C, a second activation mechanism occurs concurrently with metallic potassium formation. The product, metallic potassium, penetrates the graphite layers and expands the lattice by rapidly removing intercalated potassium. Increasing the activation temperature to 1200 °C can strongly induce the second activation process. Therefore, stronger expansion of the graphite lattice and removal of defective carbon structures can occur in the preparation of HP-CNSs.

The HP-CNSs on an alumina template have an irregular shape and various sizes; however, their morphologies are 2D-like sheet structures with a thickness of ∼20 nm and a lateral size of several micrometers [Figure 1(b and c)]. Field-emission transmission electron microscopy (FE-TEM) images revealed a high aspect ratio nanostructure for the HP-CNSs [Figure 1(d and e)]. High-resolution FE-TEM images showed an amorphous carbon structure of the HP-CNSs. The crystal structure of HP-CNSs was examined by X-ray diffraction (XRD) and Raman spectroscopy [Figure 2(a and b), respectively]. XRD revealed two broad peaks at 22.3 and 42.9° 2$\theta$, which were assigned to the degree of stacking order of the layered carbon structure (002) and ordered hexagonal carbon structure (100), respectively. These broad peaks indicated that the carbon crystallite BSU grew slightly [Figure 2(a)]. The Raman spectrum exhibited D and G band peaks at ∼1348 and ∼1605 $cm^{-1}$, respectively. The D band was assigned to disorder originating from $sp^3$ carbons, whereas the G band was associated with a hexagonal carbon structure. The ratio of the D peak intensity to the G peak intensity was $I_D/I_G$ = 1, indicating that the domain size ($L_a$) of the hexagonal carbon structure corresponded to several nanometers. Nevertheless, the electrical transport properties observed for the HP-CNSs were superior to those of reduced graphene oxide [Figure 2(c and d)].[31,32] For the temperature-dependent electrical transport properties of HP-CNSs, current−voltage ($I$−$V$) measurements showed highly symmetric, linear behavior throughout the different temperature regions. The conductivity ($\sigma(T)$) decreased with temperature [Figure 2(c)], indicating non-metallic behavior. At room temperature, the HP-CNS conductivity was 60 S $cm^{-1}$ [Figure 2(d)], which was at least 10-fold higher than that of reduced graphene oxide.[31,32] This high conductivity was attributed to doping effects of nitrogen and sulfur. Doping with nitrogen and/or sulfur modifies the conduction band, leading to a larger electron donor state.[2,32]

The porous properties of HP-CNSs were investigated by nitrogen adsorption and desorption experiments. The nitrogen adsorption and desorption isotherm curves [Figure 3(a)] are indicative of hybrid International Union of Pure and Applied Chemistry (IUPAC) Type-I and -IV shapes, suggesting the existence of domains with microporous and mesoporous structures. The IUPAC classification 2 (H2)-type hysteresis in the desorption curve suggests that mesoporous structures in HP-CNSs were not well-defined. In contrast, the isothermal curves of samples in which the WCG/KOH mixtures were heat-treated at 800 °C showed IUPAC Type-I microporous structures. The microporous carbon nanosheets (MP-CNSs) have a concentration of absorbed nitrogen at relative pressures <0.1 that is higher than that of HP-CNSs, suggesting that they have a higher micropore content. Figure 3(b) shows the micropore size distributions for the samples. MP-CNSs-0.5 (0.5 KOH to WCG content) had the largest micropores in the samples; subnanometer-sized pores (∼0.54 nm) were dominant in the pore structure. The micropore content decreased with increasing KOH to WCG content ratios. In contrast, the micropore sizes increased with increasing KOH content. HP-CNSs revealed an increase in micropore size (∼0.59 nm) despite the use of a 0.5 KOH to WCG content to fabricate the


DOI: 10.1021/am5081919
ACS Appl. Mater. Interfaces 2015, 7, 3684−3690

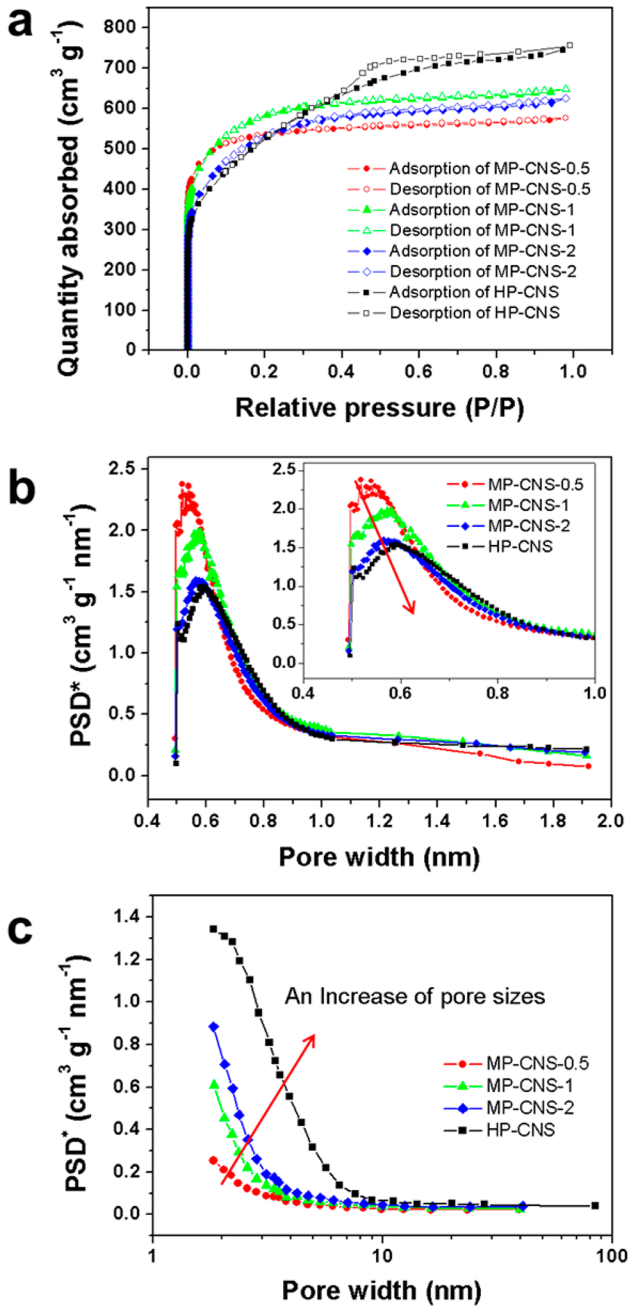


**Figure 3.** (a) Nitrogen adsorption and desorption curves of HP- and MP-CNSs with specific surface areas of 2036.2, 2110.6, and 1903.6 $m^2$ $g^{-1}$ corresponding to MP-CNS-0.5, -1, and -2, respectively. (b) Micropore and (c) mesopore size distributions of HP-CNS and MP-CNS-0.5, -1, and -2.

HP-CNSs. This tendency was evident in the mesopore size distributions [Figure 3(c)]. The HP-CNSs showed the largest mesopore size distributions in the samples, which covered a range up to ~10 nm. In addition, the micropore and mesopore volumes gradually increased with an increase in activation agents, and HP-CNSs had the highest micropore and mesopore volumes in the samples. The specific surface area of the HP-CNSs was 1945.7 $m^2$ $g^{-1}$, which was similar to the values for MP-CNSs (2036.2, 2110.6, and 1903.6 $m^2$ $g^{-1}$ for MP-CNS-0.5, -1, and -2, respectively). More information about the textural properties of the samples is described in Table S2 in the SI.

The electrochemical performance of the HP-CNS-based supercapacitors was analyzed using the organic electrolyte 1-butyl-3-methylimidazolium tetrafluoroborate acetonitrile (BMIM $BF_4$/AN) over the potential range of 0−3.0 V. The cyclic voltammograms of the HP-CNS-based supercapacitors, as shown in Figure 4(a), exhibited typical capacitive behavior with rectangular-shaped voltammetry characteristics over a wide range of voltage scan rates. The steep slopes of the current change at the switching potential indicated small mass-transfer resistance. The hierarchical pore structure of the HP-CNSs provides a well-defined ion pathway and electrolyte reservoir, allowing for rapid ionic motion. These ideal capacitive behaviors were maintained at a scan rate of 50 mV $s^{-1}$. Additionally, the galvanostatic charge/discharge curves of the HP-CNS-based supercapacitors exhibited linear charge/discharge profiles with low dynamic voltage (IR) drops and almost 100% Coulombic efficiency over a large voltage range [Figure 4(b)]. In contrast, the cyclic voltammograms of the MP-CNS-based supercapacitors revealed a distortion in the capacitive behavior with increasing scan rate. The galvanostatic charge/discharge curves exhibited a relatively large IR drop with increasing current density [Figure S5 in the SI]. Nevertheless, the electrochemical performances of the MP-CNS-based supercapacitors were superior to that of commercial activated carbon-based supercapacitors, which has a similar specific surface area (~1925 $m^2$ $g^{-1}$) and microporous structure but poor heteroatoms [Figure S6 in the SI]. These results suggest that doped nitrogen and/or sulfur heteroatoms on the carbon structure can improve the electrochemical performances. Figure 4(c) shows Nyquist plots of the HP-CNS-based supercapacitors over the frequency range from 100 kHz down to 0.1 Hz. This plot features a vertical line in the low-frequency region, indicative of ideal capacitive behavior. From the magnified data in the relatively high frequency region, a transition between the RC semicircle and the migration of the electrolyte was observed at a frequency of ~115 Hz. The ~115 to ~2.1 Hz section of the plot displayed Warburg resistance, which is the result of frequency-dependent ion diffusion in the electrolyte to electrode interface. The Warburg resistance section was very short, indicating that the electrolyte ions had efficient access to the electrode surface as shown in the inset of Figure 4(c). In contrast, the Warburg resistance regions of the MP-CNS-based supercapacitors were increased more based on decreasing pore size, clarifying the importance of hierarchical pore structure for ion diffusion [Figure S7 in the SI]. The rate capabilities of all of the samples were characterized at current densities ranging from 0.5 to 20 A $g^{-1}$ [Figure 4(d)]. The HP-CNS-based supercapacitors showed 121 F $g^{-1}$ at a current density of 0.5 A $g^{-1}$, which is lower than the 129 F $g^{-1}$ of MP-CNS-0.5-based supercapacitors. In contrast, with increasing current density, good capacitance retention was observed in the HP-CNS-based supercapacitors. At a high current density of 20 A $g^{-1}$, the HP-CNS-based supercapacitors maintained a capacitance of 55.3 F $g^{-1}$, which was ~5- and 2-fold higher than those of the MP-CNS-0.5- and MP-CNS-1-based supercapacitors, respectively. Figure 4(e) shows Ragone plots of these samples and their energy and power characteristics. The HP-CNSs showed a specific energy of 35.4 Wh $kg^{-1}$ at 11250 W $kg^{-1}$ and 23 Wh $kg^{-1}$ at a 3 s charge/discharge current rate, corresponding to a specific power of 30000 W $kg^{-1}$. These high power characteristics originated from the high aspect ratio nanostructure (20 nm thickness to several micrometers in lateral size) and a hierarchical pore structure,


DOI: 10.1021/am5081919
ACS Appl. Mater. Interfaces 2015, 7, 3684−3690

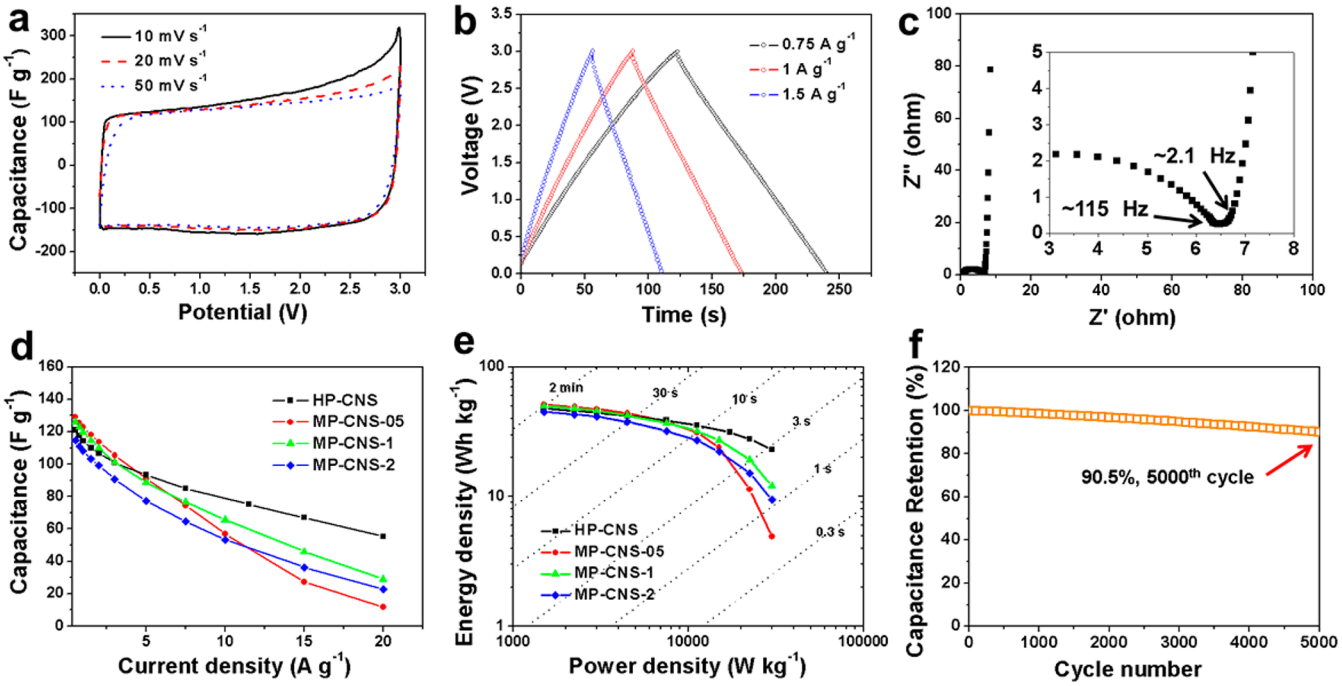


**Figure 4.** Electrochemical performance over a potential range of 0−3 V in 1-butyl-3-methylimidazolium tetrafluoroborate/acetonitrile (BMIM $BF_4$/AN) electrolytes. (a) Cyclic voltammograms of HP-CNS-based supercapacitors at scan rates of 10, 20, and 50 mV $s^{-1}$. (b) Galvanostatic charge/discharge curves of HP-CNS-based supercapacitors at current densities of 0.75, 1, and 1.5 A $g^{-1}$. (c) Nyquist plot of HP-CNS-based supercapacitors over the frequency range from 100 kHz to 0.1 Hz. (d) Specific capacitance of supercapacitors based on HP-CNS and MP-CNS-0.5, -1, and -2 measured at various current densities. (e) Ragone plots of supercapacitors based on HP-CNS and MP-CNS-0.5, -1, and -2. (f) Capacitance retention of the HP-CNS-based supercapacitors during 5000 charge/discharge cycles at a current density of 1 A $g^{-1}$.

as shown in Figure S8 in the SI. Additionally, good electrical properties and wettability contributed to efficient electron/ion transfer and the expansion of active sites, respectively. Therefore, both high energy and high power were demonstrated by the well-defined HP-CNSs fabricated using a simple synthesis process. The HP-CNS-based supercapacitors showed good capacitance retention (90.5%) over 5000 charge/discharge cycles [Figure 4(f)].

## CONCLUSION

In summary, HP-CNSs were fabricated from an exfoliated WCG/KOH mixture by in situ carbonization and activation under a HTT of 1200 °C. The HP-CNSs exhibited a 2D nanosheet morphology that was 20 nm thick and several micrometers in lateral size as well as an amorphous carbon structure containing numerous heteroatoms. The HP-CNSs also had good electrical conductivity (60 S $cm^{-1}$), a high specific surface area (1945.7 $m^2$ $g^{-1}$), and a hierarchical pore structure. The HP-CNS-based supercapacitors exhibited a specific capacitance of 121 F $g^{-1}$ at a current density of 0.5 A $g^{-1}$. A specific capacitance of 55.3 F $g^{-1}$ was maintained at a 40-fold higher current rate. As a result, a specific energy of 35.4 Wh $kg^{-1}$ at 11250 W $kg^{-1}$ was achieved with HP-CNS-based supercapacitors, which also demonstrated good cyclic performance over 5000 cycles.

## EXPERIMENTAL SECTION

**HP-CNS Fabrication.** The WCGs, obtained from commercial beverage manufacturers, were treated ultrasonically using a horn-type sonicator in *N*,*N*-dimethylformamide (99.8%, Sigma-Aldrich, USA). The supernatant was vacuum-filtered, and the solvent was exchanged using *tert*-butanol. The exfoliated WCGs were frozen at −196 °C and then freeze-dried at −45 °C and 4.5 Pa for 72 h. The exfoliated WCGs (5 g) were mixed with 2.5 g of KOH (95%, Samchun Pure Chemical Co., Ltd., Korea) in a mortar and then heated to 1200 °C for 2 h at a heating rate of 10 °C $min^{-1}$. The resulting products (HP-CNSs) were washed using distilled water and ethanol (99.9%, OCI Co., USA) and then dried in a vacuum oven at 30 °C. A similar method was used to make MP-CNSs except for the heating temperature. The exfoliated WCGs (5 g) were mixed with 2.5, 5, and 10 g of KOH in a mortar and then heated to 800 °C under the same conditions used to prepare the HP-CNSs; the resulting products, MP-CNS-0.5, -1, and -2, were washed with distilled water and ethanol and then dried in a vacuum oven at 30 °C.

**Characterization.** The morphology of the HP-CNSs was examined by field-emission scanning electron microscopy (FE-SEM, S-4300, Hitachi, Japan) and field-emission transmission electron microscopy (FE-TEM, JEM2100F, JEOL, Japan). Raman spectra were recorded using a continuous-wave linearly polarized laser (514.5 nm wavelength, 2.41 eV, 16 mW power). The laser beam was focused by a 100× objective lens, resulting in a spot ∼1 $\mu$m in diameter. The acquisition time and number of circulations to collect each spectrum were 10 s and 3, respectively. X-ray diffraction (XRD, Rigaku DMAX 2500) was carried out using Cu K$\alpha$ radiation ($\lambda$ = 0.154 nm) at 40 kV and 100 mA. The chemical composition of the samples was examined by X-ray photoelectron spectroscopy (XPS, PHI 5700 ESCA, USA) with monochromatic Al K$\alpha$ radiation ($h\nu$ = 1486.6 eV), Fourier transformed infrared spectrometer (VERTEX 80v, Bruker Optics, Germany), and elemental analysis with an EA1112 analyzer (CE Instrument, Italy). The porous properties of the samples were analyzed using nitrogen adsorption and desorption isotherms that were obtained using the surface area and a porosimetry analyzer (ASAP 2020, Micromeritics, USA) at −196 °C. The BET surface areas ($S_{BET}$) were calculated according to the Brunauer−Emmett−Teller (BET) theory. The micropore surface area ($S_{mic}$) was obtained using t-plot theory, whereas the mesopore surface area ($S_{meso}$) was calculated according to the Barrett−Johner−Halendar theory. To measure the electrical transport properties, an HP-CNS was deposited onto a 300 nm thick $SiO_2$/highly p-doped Si wafer. The electrode was fabricated


DOI: 10.1021/am5081919
ACS Appl. Mater. Interfaces 2015, 7, 3684−3690

by conventional electron beam lithography (30 keV acceleration voltage). Ti/Au (5:50 nm) was deposited using an electron gun evaporation system in high vacuum ($<1 \times 10^{-3}$ Pa) and lift-off procedures. The temperature-dependent $I-V$ characteristics were determined using the conventional two-probe method with a Janis cryogenic system and semiconductor characterization system (4200-SCS, Keithley). The electrical measurements were taken after vacuum degassing for 12 h ($<5 \times 10^{-4}$ Pa).

**Electrochemical Characterization.** Electrochemical measurements were taken using a two-electrode system consisting of two symmetric HP-CNS-based electrodes. The HP-CNSs were first mixed individually into a paste containing 5 wt % polyvinylidene fluoride (Sigma-Aldrich, USA). The electrodes (1 cm diameter, 100 $\mu$m thickness) were formed from the thick slurry and pressed onto an aluminum current collector. A 1:1 weight ratio mixture of 1-butyl-3-methylimidazolium tetrafluoroborate (BMIM $BF_4$) and acetonitrile (AN) was used as the electrolyte. The electrodes and a porous polypropylene separator (Whatman GF/F, USA) were sandwiched together in a stainless steel cell to form a two-electrode cell device. All cell preparation steps were conducted in an Ar filled glovebox; the oxygen and water levels were maintained below 1 ppm.

The electrochemical performance of the symmetric supercapacitors was characterized by cyclic voltammetry, galvanostatic charge/discharge measurements, and electrical impedance spectroscopy (EIS) (PGSTAT302N, Metrohm Autolab, The Netherlands) measurements. The specific capacitance of the symmetric supercapacitors was determined from the galvanostatic measurements using the equation

$$C = \frac{4I_{cons}}{m\, dV/dt} \quad (1)$$

where $I_{cons}$ is the (constant) current, $m$ is the total mass of both carbon electrodes, and $dV/dt$ was calculated from the slope of the discharge curve over the range from $V = V_{max}$ (the voltage at the beginning of discharge) to $V = 1/2V_{max}$. The specific power density and energy density of the supercapacitors were calculated using eqs 2−4.

$$P = \Delta V I/m \quad (2)$$

$$E = Pt/3600 \quad (3)$$

$$\Delta V = (E_{max} + E_{min})/2 \quad (4)$$

In eqs 2−4, $E_{max}$ and $E_{min}$ are the potentials (V) at the beginning and end of the discharge, respectively, $I$ is the charge/discharge current (A), $t$ is the discharge time (s), and $m$ is the total mass (kg) of the active materials, including both electrodes, in the symmetric supercapacitors. A current density ranging from 1 to 20 A $g^{-1}$ was applied to all of the cells while the potential between the two electrodes was swept between the cutoff values of 0 and 3.0 V. For the cycling test, a current density of 1 A $g^{-1}$ was applied.

## ■ ASSOCIATED CONTENT

### Supporting Information

Additional information about the HP-CNS and MP-CNS samples and commercial activated carbons. This material is available free of charge via the Internet at http://pubs.acs.org.

## ■ AUTHOR INFORMATION

### Corresponding Author

*E-mail: hjjin@inha.ac.kr.

### Notes

The authors declare no competing financial interest.

## ■ ACKNOWLEDGMENTS

This work was supported by the National Research Foundation of Korea Grant funded by the Korean government (MEST) (NRF-2010-C1AAA001-0029018) and by Basic Science Research Program through the National Research Foundation of Korea (NRF) funded by the Ministry of Education (NRF-2013R1A1A2A10008534), and by Core Technology of Materials funded by the Ministry of Trade, Industry & Energy, Republic of Korea (10050858).

## ■ REFERENCES

(1) Simon, P.; Gogotsi, Y. Materials for Electrochemical Capacitors. *Nat. Mater.* **2008**, *7*, 845−854.
(2) Yun, Y. S.; Yoon, G.; Kang, K.; Jin, H.-J. High-Performance Supercapacitors Based on Defect-Engineered Carbon Nanotubes. *Carbon* **2014**, *80*, 246−254.
(3) Yun, Y. S.; Cho, S. Y.; Shim, J.; Kim, B. H.; Chang, S.-J.; Baek, S. J.; Huh, Y. S.; Tak, Y.; Park, Y. W.; Park, S. Microporous Carbon Nanoplates from Regenerated Silk Proteins for Supercapacitors. *Adv. Mater. (Weinheim, Ger.)* **2013**, *25*, 1993−1998.
(4) Chmiola, J.; Yushin, G.; Gohotsi, Y.; Porter, C.; Simon, P.; Taberna, P. L. Anomalous Increase in Carbon Capacitance at Pore Sizes Less Than 1 Nanometer. *Science* **2006**, *313*, 1760−1763.
(5) Zhu, Y.; Murali, S.; Stoller, M. D.; Hanesh, K. J.; Cai, W.; Ferreira, P. J.; Pirkle, A.; Wallace, R. M.; Cychosz, K. A.; Thommes, M.; Su, D.; Stach, E. A.; Ruoff, R. S. Carbon-Based Supercapacitors Produced by Activation of Graphene. *Science* **2011**, *332*, 1537−1541.
(6) Miller, J. R.; Simon, P. Electrochemical Capacitors for Energy Management. *Science* **2008**, *321*, 651−652.
(7) Maier, J. Nanoionics: Ion Transport and Electrochemical Storage in Confined Systems. *Nat. Mater.* **2005**, *4*, 805−815.
(8) Lu, W.; Lieber, C. M. Nanoelectronics from the Bottom Up. *Nat. Mater.* **2007**, *6*, 841−850.
(9) Rolison, D. R.; Long, J. W.; Lytle, J. C.; Fischer, A. E.; Rhodes, C. P.; McEvoy, T. M.; Bourg, M. E.; Lubers, A. M. Multifunctional 3D Nanoarchitectures for Energy Storage and Conversion. *Chem. Soc. Rev.* **2009**, *38*, 226−252.
(10) Arico, A. S.; Bruce, P.; Scrosati, B.; Tarascon, J.-M.; Van Schalkwijk, W. Nanostructured Materials for Advanced Energy Conversion and Storage Devices. *Nat. Mater.* **2005**, *4*, 366−377.
(11) Pech, D.; Brunet, M.; Durou, H.; Huang, P.; Mochalin, V.; Gogotsi, Y.; Taberna, P.-L.; Simon, P. Ultrahigh-Power Micrometre-Sized Supercapacitors Based on Onion-Like Carbon. *Nat. Nanotechnol.* **2010**, *5*, 651−654.
(12) Diggikar, R. S.; Late, D. J.; Kale, B. B. Unusual Morphologies of Reduced Graphene Oxide and Polyaniline Nanofibers-Reduced Graphene Oxide Composites for High Performance Supercapacitor Applications. *RSC Adv.* **2014**, *4*, 22551−22560.
(13) Chen, L.-F.; Zhang, X.-D.; Liang, H.-W.; Kong, M.; Guan, Q.-F.; Chen, P.; Wu, Z.-Y.; Yu, S.-H. Synthesis of Nitrogen-Doped Porous Carbon Nanofibers as an Efficient Electrode Material for Supercapacitors. *ACS Nano* **2012**, *6*, 7092−7102.
(14) Fan, Z.; Liu, Y.; Yan, J.; Ning, G.; Wang, Q.; Wei, T.; Zhi, L.; Wei, F. Template-Directed Synthesis of Pillared-Porous Carbon Nanosheet Architectures: High-Performance Electrode Materials for Supercapacitors. *Adv. Energy Mater.* **2012**, *2*, 419−424.
(15) Yun, Y. S.; Im, C.; Park, H. H.; Hwang, I.; Tak, Y.; Jin, H.-J. Hierarchically Porous Carbon Nanofibers Containing Numerous Heteroatoms for Supercapacitors. *J. Power Sources* **2013**, *234*, 285−291.
(16) Yang, S.-Y.; Chang, K.-H.; Tien, H.-W.; Lee, Y.-F.; Li, S.-M.; Wang, Y.-S.; Wang, J.-Y.; Ma, C.-C. M.; Hu, C.-C. Design and Tailoring of a Hierarchical Graphene-Carbon Nanotube Architecture for Supercapacitors. *J. Mater. Chem.* **2011**, *21*, 2374−2380.
(17) Lei, Z.; Christov, N.; Zhao, X. S. Intercalation of Mesoporous Carbon Spheres between Reduced Graphene Oxide Sheets for Preparing High-Rate Supercapacitor Electrodes. *Energy Environ. Sci.* **2011**, *4*, 1866−1873.
(18) Guo, C. X.; Li, C. M. A Self-Assembled Hierarchical Nanostructure Comprising Carbon Spheres and Graphene Nanosheets for Enhanced Supercapacitor Performance. *Energy Environ. Sci.* **2011**, *4*, 4504−4507.


DOI: 10.1021/am5081919
*ACS Appl. Mater. Interfaces* 2015, 7, 3684−3690

(19) Li, Y.; Li, Z.; Shen, P. K. Simultaneous Formation of Ultrahigh Surface Area and Three-Dimensional Hierarchical Porous Graphene-Like Networks for Fast and Highly Stable Supercapacitors. *Adv. Mater. (Weinheim, Ger.)* **2013**, *25*, 2474−2480.
(20) Kim, B.-H.; Yang, K. S.; Ferraris, J. P. Highly Conductive, Mesoporous Carbon Nanofiber Web as Electrode Material for High-Performance Supercapacitors. *Electrochim. Acta* **2012**, *75*, 325−331.
(21) Liu, H.-J.; Wang, X.-M.; Cui, W.-J.; Dou, Y.-Q.; Zhao, D.-Y.; Xia, Y.-Y. Highly Ordered Mesoporous Carbon Nanofiber Arrays from a Crab Shell Biological Template and Its Application in Supercapacitors and Fuel Cells. *J. Mater. Chem.* **2010**, *20*, 4223−4230.
(22) Jenkins, R. W.; Stageman, N. E.; Fortune, C. M.; Chuck, C. J. Effect of the Type of Bean, Processing, and Geographical Location on the Biodiesel Produced from Waste Coffee Grounds. *Energy Fuels* **2014**, *28*, 1166−1174.
(23) Namane, A.; Mekarzia, A.; Benrachedi, K.; Belhaneche-Bensemra, N.; Hellal, A. Determination of the Adsorption Capacity of Activated Carbon Made from Coffee Grounds by Chemical Activation with $ZnCl_2$ and $H_3PO_4$. *J. Hazard. Mater.* **2005**, *B119*, 189−194.
(24) Boudrahem, F.; Soualah, A.; Aissani-Benissad, F. Pb(II) and Cd(II) Removal from Aqueous Solutions Using Activated Carbon Developed from Coffee Residue Activated with Phosphoric Acid and Zinc Chloride. *J. Chem. Eng. Data* **2011**, *56*, 1946−1955.
(25) Rufford, T. E.; Hulicova-Jurcakova, D.; Fiset, E.; Zhu, Z.; Lu, G. Q. Double-Layer Capacitance of Waste Coffee Ground Activated Carbons in an Organic Electrolyte. *Electrochem. Commun.* **2009**, *11*, 974−977.
(26) Rufford, T. E.; Hulicova-Jurcakova, D.; Zhu, Z.; Lu, G. Q. Nanoporous Carbon Electrode from Waste Coffee Beans for High Performance Supercapacitors. *Electrochem. Commun.* **2008**, *10*, 1594−1597.
(27) Jisha, M. R.; Hwang, Y. J.; Shin, J. S.; Nahm, K. S.; Prem Kumar, T.; Karthikeyan, K.; Dhanikaivelu, N.; Kalpana, D.; Renganathan, N. G.; Manuel Stephan, A. Electrochemical Characterization of Supercapacitors Based on Carbons Derived from Coffee Shells. *Mater. Chem. Phys.* **2009**, *115*, 33−39.
(28) Marsh, H.; Rodríguez-Reinoso, F. *Activated Carbon*; Elsevier: Oxford, U.K., 2006.
(29) Romanos, J.; Beckner, M.; Rash, T.; Firlej, L.; Kuchta, B.; Yu, P.; Suppes, G.; Wexler, C.; Pfeifer, P. Nanospace Engineering of KOH Activated Carbon. *Nanotechnology* **2012**, *23*, 15401.
(30) Dumanlı, A. G.; Windle, A. H. Carbon Fibres from Cellulosic Precursors: a Review. *J. Mater. Sci.* **2012**, *47*, 4236−4250.
(31) Gómez-Navarro, C.; Weitz, R. T.; Bittner, A. M.; Scolari, M.; Mews, A.; Burghard, M.; Kern, K. Electronic Transport Properties of Individual Chemically Reduced Graphene Oxide Sheets. *Nano Lett.* **2007**, *7*, 3499−3503.
(32) Yun, Y. S.; Le, V.-D.; Kim, H.; Chang, S.-J.; Baek, S. J.; Park, S.; Kim, B. H.; Kim, Y.-H.; Kang, K.; Jin, H.-J. Effects of Sulfur Doping on Graphene-Based Nanosheets for Use as Anode Materials in Lithium-Ion Batteries. *J. Power Sources* **2014**, *262*, 79−85.


DOI: 10.1021/am5081919
*ACS Appl. Mater. Interfaces* 2015, 7, 3684−3690